crystals

MDPI

Article

NAi/Li Antisite Defects in the $Li_{1.2}Ni_{0.2}Mn_{0.6}O_2$ Li-Rich Layered Oxide: A DFT Study

Mariarosaria Tuccillo [1], Angelo Costantini [1], Arcangelo Celeste [1], Ana Belén Muñoz García [2,3], Michele Pavone [3,4], Annalisa Paolone [5], Oriele Palumbo [5] and Sergio Brutti [1,3,*]

1 Department of Chemistry, University of Rome La Sapienza, Piazzale Aldo Moro 5, 00185 Rome, Italy; mariarosaria.tuccillo@uniroma1.it (M.T.); costantini.1755237@studenti.uniroma1.it (A.C.); arcangelo.celeste@uniroma1.it (A.C.)
2 Department of Physics, University of Naples Federico II, Via Cintia 21, 80126 Napoli, Italy; anabelen.munozgarcia@unina.it
3 GISEL-Centro di Riferimento Nazionale per i Sistemi di Accumulo Elettrochimico di Energia, INSTM via G. Giusti 9, 50121 Firenze, Italy; michele.pavone@unina.it
4 Department of Chemical Sciences E. Pancini, University of Naples Federico II, Via Cintia 21, 80126 Napoli, Italy
5 Consiglio Nazionale delle Ricerche, Istituto dei Sistemi Complessi, Piazzale Aldo Moro 5, 00185 Rome, Italy; annalisa.paolone@roma1.infn.it (A.P.); oriele.palumbo@roma1.infn.it (O.P.)
* Correspondence: sergio.brutti@uniroma1.it; Tel.: +39-0649913957

Abstract: Li-rich layered oxide (LRLO) materials are promising positive-electrode materials for Li-ion batteries. Antisite defects, especially nickel and lithium ions, occur spontaneously in many LRLOs, but their impact on the functional properties in batteries is controversial. Here, we illustrate the analysis of the formation of Li/Ni antisite defects in the layered lattice of the Co-free LRLO $Li_{1.2}Mn_{0.6}Ni_{0.2}O_2$ compound through a combination of density functional theory calculations performed on fully disordered supercells and a thermodynamic model. Our goal was to evaluate the concentration of antisite defects in the trigonal lattice as a function of temperature and shed light on the native disorder in LRLO and how synthesis protocols can promote the antisite defect formation.

Keywords: lithium-rich layered oxides; Li-ion battery; density functional theory; materials thermodynamics

Citation: Tuccillo, M.; Costantini, A.; Celeste, A.; García, A.B.M.; Pavone, M.; Paolone, A.; Palumbo, O.; Brutti, S. NAi/Li Antisite Defects in the $Li_{1.2}Ni_{0.2}Mn_{0.6}O_2$ Li-Rich Layered Oxide: A DFT Study. *Crystals* **2022**, *12*, 723. https://doi.org/10.3390/cryst12050723

Academic Editor: Sławomir Grabowski

Received: 21 April 2022
Accepted: 16 May 2022
Published: 19 May 2022

1. Introduction

Computational techniques applied to study active components and processes in secondary aprotic batteries, such as Li-ion cells, are powerful tools used to evaluate the underlying fundamental chemistry and electrochemistry [1–4]. Density functional theory calculations are typically carried out to outline materials' physico-chemical, thermal and electrochemical properties, as well as thermodynamic stabilities and ionic or electronic conductivities [4–7]. Overall, computational productions can pave the way for a rational design of materials and can help the understanding of complex phenomena in batteries, such as voltage hysteresis, voltage decay or anionic redox reactions in superlattices [8–10].

Current trends concerning the application of computational materials science to secondary battery research follow the parallel experimental material developments, thus focusing on the redox-active components, either negative or positive electrodes, as well as electrolytes and interfaces [11–16].

State-of-the-art positive-electrode materials used in Li-ion batteries are based on mixed-transition-metal-layered oxides (TMLOs) [17–19]; this class of compounds is an excellent example of stable and long-lasting redox-active intercalation materials. However, all TMLOs suffer from a limited capacity, which is always below 160–180 $mAhg^{-1}$, and typically contain large amounts of cobalt, a well-known critical raw material [20,21]. Among the many possible

alternatives to TMLOs, lithium-rich layered oxides (LRLOs) demonstrate outstanding improvements in terms of specific capacity, i.e., above 220–240 $mAhg^{-1}$ [7,22–26]. Furthermore, a careful balancing of the metal blend in the general $Li_{1+x}M_{1-x}O_2$ (M = metal blend) stoichiometry allows a complete Co removal from the phase, with minor effects on stability and reversibility [23,27], despite the destabilization of the magnetic ordering and the induced electronic disorder [7].

Similar to TMLOs, LRLOs are layered materials constituted by a regular stacking along the c axis of planar atomic sheets, with the sequence M-O-Li-O. In the case of TMLOs, the hexagonally packed M layer is occupied only by transition metals, whereas in the case of an ideal LRLO mC24 monoclinic lattice, the atomic sites on the M layers are occupied by a blend of metals (typically Mn/Ni/Co with minor dopants) surrounding lithium ions in quasi-regular LiM_6 hexagonal motifs. However, LRLO lattices are inherently disordered and defective due to the peculiarity of their stoichiometry and structure [28,29], further driven by the local fluctuations in the transition metals in the M layer. Thus, the ideal mC24 lattice incorporates large concentrations of 0D antisite defects (in-plane and out-of-plane) mixing Li and TM ions, 0D voids (in both cationic and anionic sublattice) and 2D stacking faults [23,30,31]. Such massive alteration in the monoclinic translational symmetry along the (a,b) in-plane lattice vectors as well as along the c-stacking axis (ideal mC24 staking: ABAB) results in an apparent trigonal lattice hR12 [28,30,32]. In fact, the hR12 prototype structure is able to better mimic the quasi-random occupancy of atomic sites in the M layer by Li and TM ions, as well as the occurrence of stacking faults in the ideal mC24, being the hR12 staking sequence ABCABC [7,25,28,32–37].

Whereas in-plane M/Li antisites break the monoclinic symmetry, off-plane antisite defects, which switch transition metals from the M layer with lithium ions from the Li layer, can alter remarkably the physico-chemical properties of the lattice [30,38–43]. In particular, Ni^{2+} ions are dimensionally very similar to Li^+ ions (0.69 vs. 0.76 Å, respectively), compared to Co^{3+} (0.6 Å), Mn^{4+} (0.53 Å) or Fe^{3+} (0.55 Å), thus making likely their antisite switch with Li^+ thanks to the minor steric distortions in the surrounding coordination shell [41,42].

Generally speaking, antisite defects occur in an alloy or ordered compound when two different types of atoms sitting in different atomic sites of the crystal structure switch positions [44]. In LRLOs, the occurrence of small concentration of Ni/Li antisites helps the structural resilience of the lattice under large de-intercalation of Li^+ ions, above 0.6–0.7 equivalents. In the literature, this beneficial effect is known as the pillar effect [45] and can help increase the reversible specific capacity upon cycling in batteries. On the other hand, at large concentrations, the presence of Ni^{2+} ions in the Li^+-ion layers can modify the ion diffusion in the material, leading to possible kinetic barriers to the de-intercalation/intercalation [41,42,45].

In this communication, we present a thermodynamic analysis concerning the out-of-plane Ni/Li antisite defect formation in a Co-free LRLO material, with stoichiometry $Li_{1.2}Ni_{0.2}Mn_{0.6}O_2$, derived using first-principles calculations based on the density functional theory (DFT). Starting from an hR12 unit cell [23,24], here we studied a 5x2x1 supercell containing 120 atoms ($Li_{36}Ni_6Mn_{18}O_{60}$, namely LNM, having a stoichiometry equivalent to $Li_{1.2}Ni_{0.2}Mn_{0.6}O_2$) as shown in Figure 1a. This 5x2x1 hR12 superstructure consisted of a regular ABC stacking of almost-planar layers containing Li/O/M/O species, respectively (M = weighted blend of Li/Mn and Ni atoms); this superstructure is free from out-of-plane Ni/Li antisite defects, whereas the M layer is fully disordered, randomly mixing Mn/Ni and Li ions. The occurrence of out-of-plane Ni/Li antisite defects is therefore mimicked by switching Ni and Li close pairs.

Our goal is to outline the fundamental thermodynamics of the antisite defect formation, their impact on the electronic properties, local coordination environment as well as lattice stability. Starting from DFT calculations, here we illustrate the evolution at a finite temperature of the antisite concentration; this information can help in a rational evaluation of the impact of high-temperature annealing on the defectivity of LRLOs.

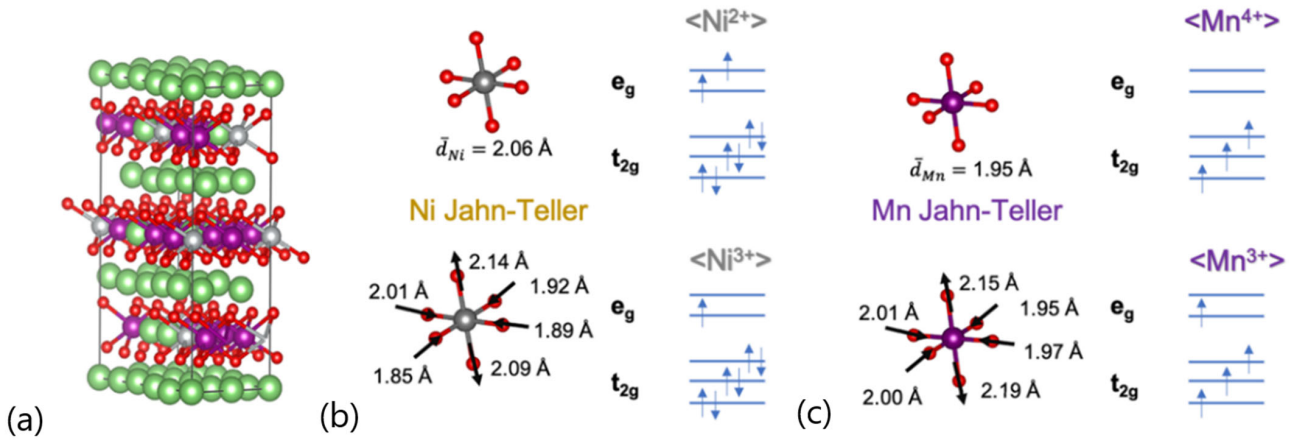

Figure 1. (**a**) Optimized geometry and volume structures supercell 5 × 2 × 1 containing 120 atoms of $Li_{1.2}Ni_{0.2}Mn_{0.6}O_2$ (LNM) phase; (**b**) Ni-O and (**c**) Mn-O bond distances also considering Jahn–Teller centers. Color code: Li—green, Ni—gray, Mn—violet, O—red.

It is important to underline that Ni/Li antisite defects can form in any layered lattice where Ni^{2+} ions are present, due to the similar ionic radium compared to Li^+. In this respect, this study sheds light on a structural feature also common in other usual LRLO stoichiometries, such as the nickel-rich ternary $LiNi_xCo_yMn_zO_2$ (NCM; $0.5 \leq x < 1$, $x + y + z = 1$) [46,47]. Furthermore, antisite disorder can also play a relevant role upon cycling in many layered and LRLO cathodes for LIBs. In fact, Ni/Li switch defects can also occur in parallel to other possible degrading mechanisms that affect LRLOs in batteries [48], such as side reactions between LRLO oxides and the aprotic electrolytes [49], the surface crystallographic reconstruction during repeated de-insertion/insertion cycles [50] and the pulverization of the secondary particle agglomerates [51].

2. Methods

2.1. Computational Method

All calculations were performed with the Vienna Ab-initio Simulation Package (VASP), which performs periodic ab initio quantum mechanical calculations within the Kohn–Sham DFT [44,45] framework, with projector-augmented wave potentials and plane wave basis sets. We applied the generalized-gradient approximation (GGA) [46] with the exchange–correlation density functional by Perdew, Burke and Ernzenhof (PBE) [47].

We used the DFT + U method [48], which has been extensively validated for correcting large self-interaction errors in transition-metal oxides [49], caused by the approximate form of standard exchange–correlation density functional when applied to strongly localized unpaired electrons such as in the d manifold of Ni and Mn. An effective value of U−−J = 4.00 eV was used for all Co, Ni and Mn d electrons. This value is an average of the values of Mn and Ni reported from ab initio UHF calculations and was recently validated by us for LiMO2 layered phases (M = Ni, Mn) [4]. We used a kinetic energy cut-off of 520 eV and a Γ-centered k-point mesh at Γ. We optimized the structural parameters of supercells by relaxing iteratively the ion positions and the cell lattices without any symmetry constraints until the residual force on each atom was <0.01 eV $Å^{-1}$.

The structure of non-defective Li-rich layered oxides (LRLOs) with the formula $Li_{1.2}Ni_{0.2}Mn_{0.6}O_2$ (LNM) was built starting from the hR12 prototype unit cell and using a 5x2x1 supercell. To model transition-metal disorder in a multicomponent TM layer in the LNM supercell, we adopted the special quasi-random structure (SQS) approach [50–52]; this method allowed us to model a random solid solution in a supercell of the desired size by mimicking random correlation functions through nearest-neighbor, next-nearest-neighbor interactions and so on. The SQS method relies on the cluster expansion (CE) formalism proposed by Mayer [53]. We used the ATAT suite (Alloy Theoretic Automated

Toolkit) that exploits an SQS-based algorithm in search for a fully randomized distribution of Ni, Mn and Li ions in the TM layers within the LNM supercell [54].

The antisite defect formation was mimicked by switching one nickel atom in the TM layer with one lithium atom in the Li layer in the supercell. Within the LNM supercell, there were six inequivalent Ni atoms that could switch position with the six close-neighbor lithium atoms on the closest Li layer (three Li^+ on the upper Li layer and three Li^+ on the lower Li layer, stacked along the c axis). Thus, besides the pristine defect-free supercell, we computed 36 defective supercells, each with a single antisite defect. All configurations, without and with antisite defects, were relaxed with respect to cell parameters and atomic positions to find the corresponding ground-state structure.

Overall, by assuming an hR12-based supercell with random occupancy of the transition-metal layer, our approach allowed us to model explicitly the formation of an antisite defect in a realistic LRLO lattice.

2.2. Thermodynamic Model

Starting from the cohesion energetics calculated at the DFT level of all supercells, it was possible to calculate the energy of formation of the nickel/lithium antisite defects ($\Delta_f E$) by evaluating the energy variation between the defective supercell and the defect-free one, following Equation (1):

$$\Delta_f E = E_{Ni_i/Li_i} - E_{\mathrm{LNM}} - \sum_i^4 \Delta n_i \mu_i + q\varepsilon_F \quad (1)$$

where E indicates the cohesion energies obtained from DFT calculations: in particular, E_{Ni_i/Li_i} is the energy of the defective structure and E_{LNM} the non-defective one; Δn_i is the change in the number of atoms of the i-th species contained in LRLO caused by the formation of the defect; μ_i is the chemical potential of the i-th species contained in the studied compound; and $q\varepsilon_F$ is the product between the charge introduced into the structure due to the formation of the defect and the level of restraints of LRLO. The formation of antisite defects does not alter the number of atoms or electrons in the structure; therefore, the antisite defect formation energy can be simplified as follows:

$$\Delta_f E = E_{Ni_i/Li_i} - E_{\mathrm{LNM}} \quad (2)$$

The dependence of the concentration of the antisite defect on the temperature can be modeled assuming a simple thermodynamic model assuming that the occurrence of Li/Ni switches follows a Boltzmann statistic. Generally speaking, for any crystalline structure, a formation equilibrium can be written for any defect. For antisite defects, the formation equilibrium can be represented by Equation (3):

$$Cell \leftrightarrow (Li_{Ni})^- + (Ni_{Li})^+ \quad (3)$$

where *Cell* is the non-defective structure (LNM), $(Li_{Ni})^-$ is the negatively charged antisite defect generated by the occupancies of a Li^+ ion in a –2-charged nickel vacancy, and $(Ni_{Li})^+$ is the positively charged antisite defect generated by the occupancies of a Ni^{+2} ion in a +1-charged lithium vacancy. In a Ni/Li exchange, the defects $(Li_{Ni})^-$ and $(Ni_{Li})^+$ occur simultaneously, and therefore two antisites do not alter the number of electrons in the crystal lattice, only their distribution. For the equilibrium just described, it is possible to write an equilibrium constant, as shown in Equation (4):

$$K = \frac{\frac{n_{(Li_{Ni})^-}}{V_{cell}} * \frac{n_{(Ni_{Li})^+}}{V_{cell}}}{\frac{n_{Ni}}{V_{cell}} * \frac{n_{Li}}{V_{cell}}} = \frac{C_{(Li_{Ni})^-} * C_{(Ni_{Li})^+}}{C_{Ni} * C_{Li}} = \frac{C^2}{C_{Ni} * C_{Li}} \quad (4)$$

where $n_{(Li_{Ni})^-}$ is the number of Li antisite defects, $n_{(Ni_{Li})^+}$ is the number of Ni defects, n_{Ni} is the number of Ni atoms that occupy the lattice nodes within the TM layer, n_{Li} is the number

of Li atoms that occupy the lattice nodes within the Li layer, V_{cell} is the average volume of the supercell, and C is the corresponding defect/atom concentration. In particular, C is the concentration per volume of defects, whereas C_{Ni} and C_{Li} are the concentration per volume of nickel and lithium atoms, respectively, occupying their "perfect" crystal atomic site (i.e., C_{Ni} = 0.0056 A^{-3} and C_{Li} = 0.0284 A^{-3}). Under equilibrium conditions, the concentration of antisite defects per unit volume can be related to the defect Gibbs energy of formation through the equation:

$$C(T) = \sqrt{C_{Ni} * C_{Li}} exp\left(-\frac{\Delta_f G}{2RT}\right) \quad (5)$$

where $C(T)$ is the defect concentration per volume as a function of the temperature. $\Delta_f G$ is the defect formation free energy change that can be approximated by Equation (6):

$$\Delta_f G = \frac{\sum_{i=1}^{36} \Delta_f E_i}{36} * N_A - T \cdot \Delta_{conf} S \quad (6)$$

as the mean among the energy of formation of the 36 defective configurations (see above) and under the assumption of negligible differential thermal effects [7,55]. The term $\Delta_{conf} S$ is the variation in the configurational entropy induced by the formation of the antisite defect. By considering the LRLO supercell atomic composition (see above in the methodological section), the variation in the configurational entropy is given by:

$$\Delta_{conf} S = S_{conf,defective\ cell} - S_{conf,defect-free\ cell} \quad (7)$$

where $S_{conf,defective\ cell}$ is the configurational entropy of the defective supercell, and $S_{conf,defect-free\ cell}$ is the configuration entropy of the defect-free supercell, given by

$$S_{conf,defect-free\ cell} = -R \cdot \left(\frac{6}{30} \ln \frac{6}{30} + \frac{6}{30} \ln \frac{6}{30} + \frac{18}{30} \ln \frac{18}{30}\right) \quad (8)$$

$$S_{conf,defective\ cell} = -R \cdot \left(\frac{7}{30} \ln \frac{7}{30} + \frac{5}{30} \ln \frac{5}{30} + \frac{18}{30} \ln \frac{18}{30} + \frac{1}{30} \ln \frac{1}{30} + \frac{29}{30} \ln \frac{29}{30}\right) \quad (9)$$

where R is the gas constant. The resulting change in the configurational entropy is $\Delta_{conf} S$ = 1.1 J K^{-1}mol at^{-1}, and it is, by definition, temperature-independent.

3. Results

Despite the absence of imposed symmetry or other computational constraints during electronic and structural relaxations, the defect-free LRLO structure preserved its trigonal lattice, as shown in Table 1, where the modeled crystallographic properties are compared to the experimental data. The relaxed structural parameters have been reduced to the hR12 unit to facilitate the comparison.

Computational predictions of the cell parameters agree within 1.5% with respect to experiments and calculations [7], thus confirming the accuracy and reliability of our modeling approach. The analysis of the magnetic moments of transition metals summarized in Table 1 allows us to shed light on their corresponding oxidation states. The majority of Ni ions can be assigned to a +2 oxidation state in a low-spin (LS) configuration, with a moderate atomic fraction of 16.7% of Ni ions showing +3 oxidation state in the LS electronic configuration. The magnetic moments on Mn mainly suggest a +4 oxidation state in the high-spin (HS) electronic configuration, apart from a minor fraction (atomic fraction of 5.56%) showing a +3-oxidation state in the HS configuration. Both Ni^{3+} and Mn^{3+} are Jahn–Teller (JT) ions [52]. The electronic structure underneath the local octahedral coordination MO_6 in the hR12 lattice is represented by the occupancy of the t_{2g} and e_g bands in the crystal field. In particular, e_g orbitals overlapped the transition metal d_{z2}/d_{x2-y2} and the oxygen p states. The pictorial representation of the occupancy of the t_{2g} and e_g orbitals

is presented with the JT and non-JT octahedra in Figure 1b,c. In both JT $(Ni^{3+})O_6$ and $(Mn^{3+})O_6$ octahedra, the partial occupancy of the e_g orbitals led to the alteration in the oxygen–metal bond lengths compared to the non-JT configurations; as expected, our model suggests that axial bond lengths elongated, whereas the four equatorial bond lengths shrunk, as shown in Figure 1b,c. It is important to underline that the occurrence of JT defects was an additional source of local modulations' bond lengths and coordination shells that further contributed to the structural disorder within the LRLO lattice.

Table 1. Computed structural parameters and electronic structure analysis of the magnetic moments in the optimized defect-free LNM phase: weighted means of $\overline{\mu}_{Ni}$ and $\overline{\mu}_{Mn}$ and values for Jahn–Teller centers. The experimental values are reported in parentheses.

	Rhombohedral Unit Cell Parameters
	LNM Defect-Free (Unit Cell Angles α = β = 90°, γ = 120°)
a (Å)	2.930 (2.907) [7]
c (Å)	14.22 (14.498) [7]
$V(hR12)$ (Å^3/f.u.)	35.26 (35.36) [7]
	Electronic Structure: Magnetic Moments
$\overline{\mu}_{Ni}$	Mean value: 1.555 μ_B (i.e., Ni^{2+}) 16.7% of nickel ions show 1.001 μ_B (i.e., Ni^{3+}; Jahn–Teller)
$\overline{\mu}_{Mn}$	Mean value: 3.249 μ_B (i.e., Mn^{4+}) 5.56% of manganese ions show 3.890 μ_B (i.e., Mn^{3+}; Jahn–Teller)

The electronic structure of the defect-free LNM lattice is shown in Figure 2 in terms of atomic projected density of states (PDOS). The defect-free LNM supercell showed a zero-bandgap semiconductor character and a strong hybridization of Ni d states and Mn d states at the Fermi energy with the p states of the oxygen anions.

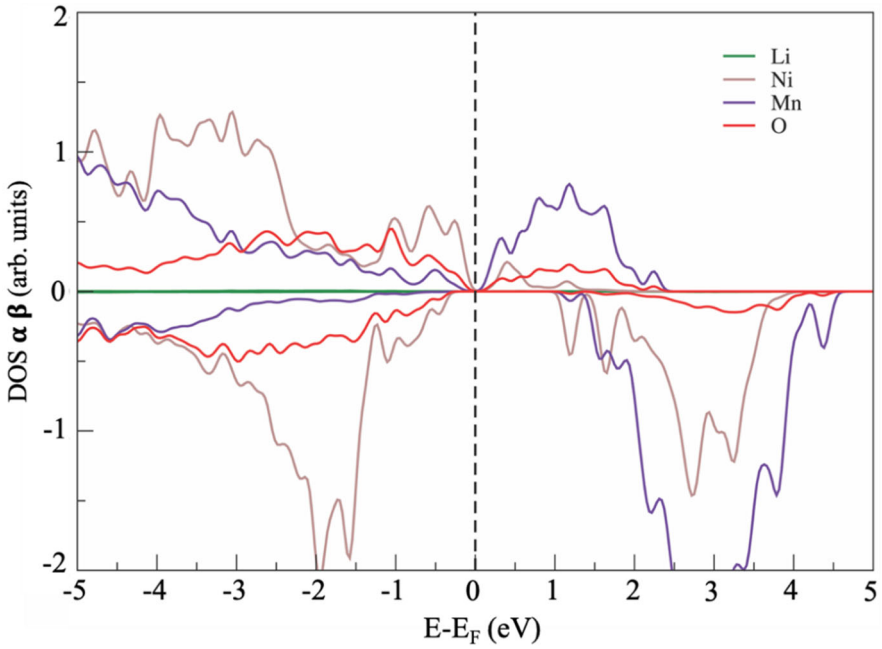

Figure 2. Atom-projected density of state (PDOS) for optimized $Li_{1.2}Ni_{0.2}Mn_{0.6}O_2$ (LNM) phase.

Starting from this defect-free LNM supercell, we computed the stability of all the 36 defective configurations where a nickel atom in the TM layer was switched with a Li atom in the Li layer (see above for more details), as pictorially represented in Figure 3, where the defect formation energy $\Delta_f E$ of each configuration is also shown.

The six atomic sites occupied by nickel ions in the non-defective supercell ($Ni_{1\ to\ 6}$) were homogeneously distributed in pairs on the three TM layers (TM1, TM2 and TM3, see Figure 3), staked along the c axis. Each antisite switch can occur by exchanging one nickel ion with one of the six Li^+ first neighbors distributed on the two vicinal Li layers, three above and three below.

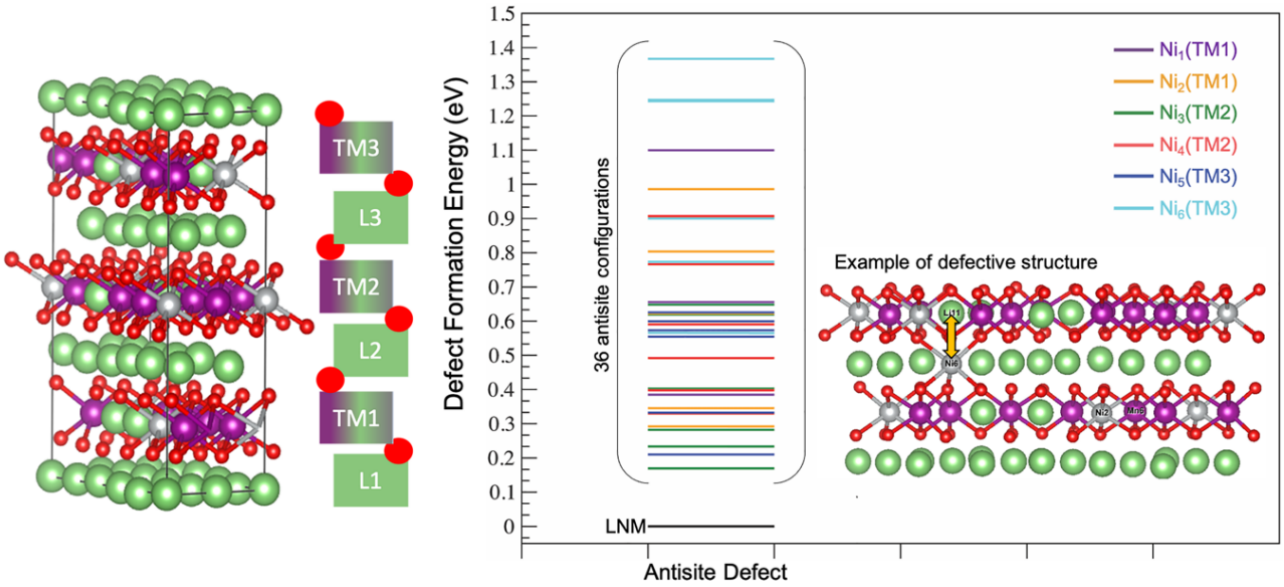

Figure 3. Defect formation energy for all defective LNM configurations. An example of a Ni/Li antisite switch is shown between a nickel atom in the TM layer and a Li atom in the Li layer.

From a thermodynamic point of view, all 36 antisite defective configurations were less stable than the parent antisite-free LNM supercell. The average energy of formation of the antisite defect was therefore positive, in line with previous studies on similar structures already present in the literature [34]. The formation energy of a single antisite defect in the supercell ranged between 0.17 and 1.37 eV, and the corresponding mean antisite formation energy was $\overline{\Delta_f E}$ = 0.62 eV.

The largest defect formation energies were given by the six switches of Ni_6, which is a JT Ni^{3+} center. This effect was expected since the Ni^{3+} ion has an ionic radium of 0.56 Å, much smaller compared to both Li^+ and Ni^{2+}, i.e., 0.69 vs. 0.76, respectively [53,54]. In fact, to accommodate the larger Li^+ in the small Ni^{3+} interstice to form the antisite, the surrounding oxygen coordination shell needs to expand, while losing the coulombic stabilization provided by the 3+ charge [55]; this combination of a steric and electrostatic effect is poorly counterbalanced by the accommodation of the smaller Ni^{3+} in the large interstice of the Li^+, thus leading to a remarkable destabilization of the lattice.

On the other hand, Ni_3 showed the lowest defect formation energy; this favorable energetics is apparently related to the composition of the second-neighbors coordination shell on the metal-layer close to the nickel atomic site. In fact, the Ni_3 atomic site was surrounded by Mn (66.67%) and Li (33.33%) atoms, whereas for all the other $Ni_{1,2,4,5,6}$ centers, at least one other Ni atom was found in the second-neighbors coordination shell. Given the peculiar coordination shell of Ni_3, only a negligible structural distortion occurred after the formation of the antisite defect, resulting in a null variation in all octahedral LiO_6 and NiO_6 bond distances.

Overall, considering all the 36 defective configurations, the mean change in the supercell volume induced by the defect formation was 0.03%, thus suggesting a negligible volumetric effect. This computational evidence unavoidably implies an elusive impact of the formation of antisite defects on the elastic scattering of light, thus making difficult their identification and quantification by X-ray diffractometry (XRD), a typical technique used to quantify antisite concentrations [38,39,56,57].

The formation of antisite defects slightly alters the electronic structure of the materials at the Fermi energy; an example of the electronic structure of a defective LNM supercell is shown in Figure 4.

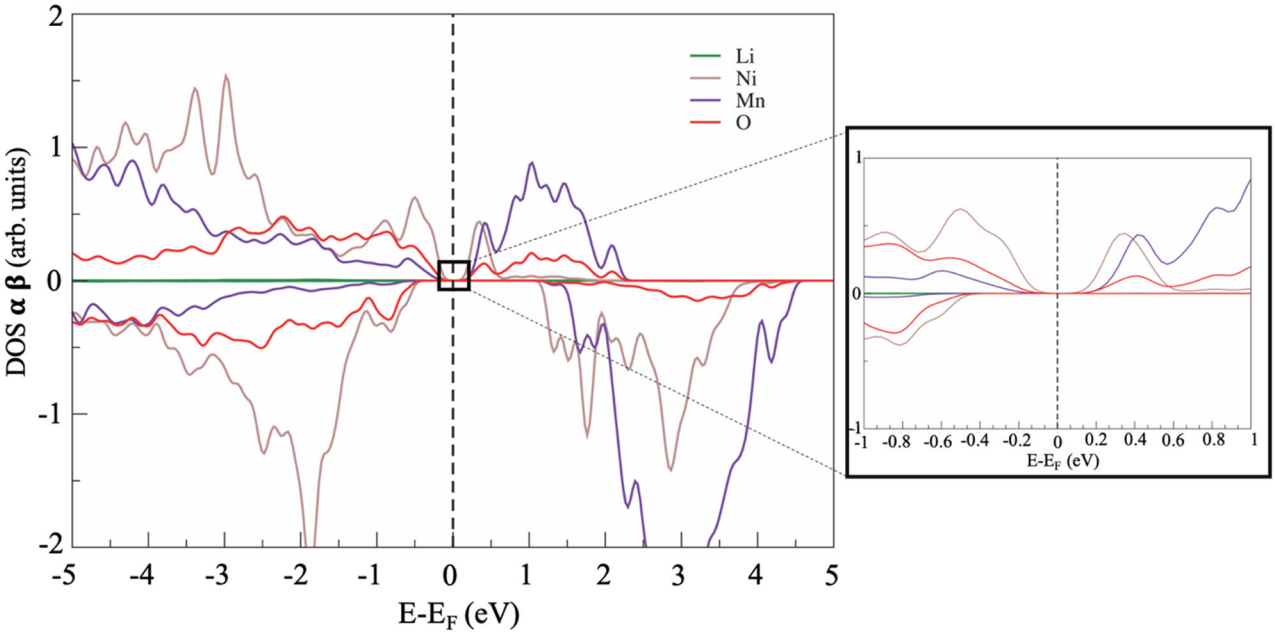

Figure 4. Example of the PDOS of LNM phase with antisite defect between Ni and Li.

Overall, the electronic structures were very similar in the defect-free and defective supercells apart from a minor feature close to the Fermi energy. Apparently, all defective structures showed a small bandgap of approximately 10–15 meV (see the inset of Figure 4), whereas the defect-free cell was a zero-bandgap material (see Figure 2). This computational prediction suggests a possible slight decrease in the electronic conductivity of LRLO induced by large antisite defectivity.

4. Discussion

The energetics of formation of antisite defects allow us to model the equilibrium concentration as a function of the temperature. The temperature trends of the antisite defect concentration normalized by the cell volume ($C_{antisite}(Å^{-3})$) or by formula unit ($C_{antisite}(f.u.^{-1})$) are shown in Figure 5.

To facilitate the comprehension of defect concentration and correlate it with structural parameters, we also estimated the mean distance between multiple antisite defects and the fraction of nickel ions that occupied an antisite position, instead of the expected crystallographic site. The estimate of the closest distance $\langle d \rangle$ between multiple antisite pairs is given by:

$$\langle d \rangle \sim \frac{a/A}{\sqrt[3]{C(T)/A^{-3} \cdot V(hR12)/A^3}} \quad (10)$$

where a/A is the corresponding hR12 lattice constant, $V(hR12)$ is the hR12 cell volume, and C(T) is the numerical defect concentration per A^3. Equation (10) can be derived by considering that the defect concentration per hR12 unit cells is $C(T)/hR12^{-1} = C(T)/A^{-3} \cdot V(hR12)/A^3$, and the number of hR12 unit cells per defect is its reciprocal ($N_{hR12}(T) = 1/\left(C(T)/hR12^{-1}\right)$). Once $N_{hR12}(T)$ is derived, by assuming a cubic 3D packing of hR12 cells to form a finite volume of crystal containing a single defect, the closest distance can be obtained by Equation (10), considering that the c cell constant along the stacking axis is much larger compared to the in-plane a lattice parameter.

The fraction of nickel ions that occupied an antisite position instead of the expected crystallographic site ($\chi_{Ni,antisite}$) is given by:

$$\chi_{Ni,antisite} = \frac{C(T)}{C_{Ni}} \quad (11)$$

where C_{Ni} = 0.0056 A^{-3} is the concentration per unit volume of the nickel atoms in the LRLO structure.

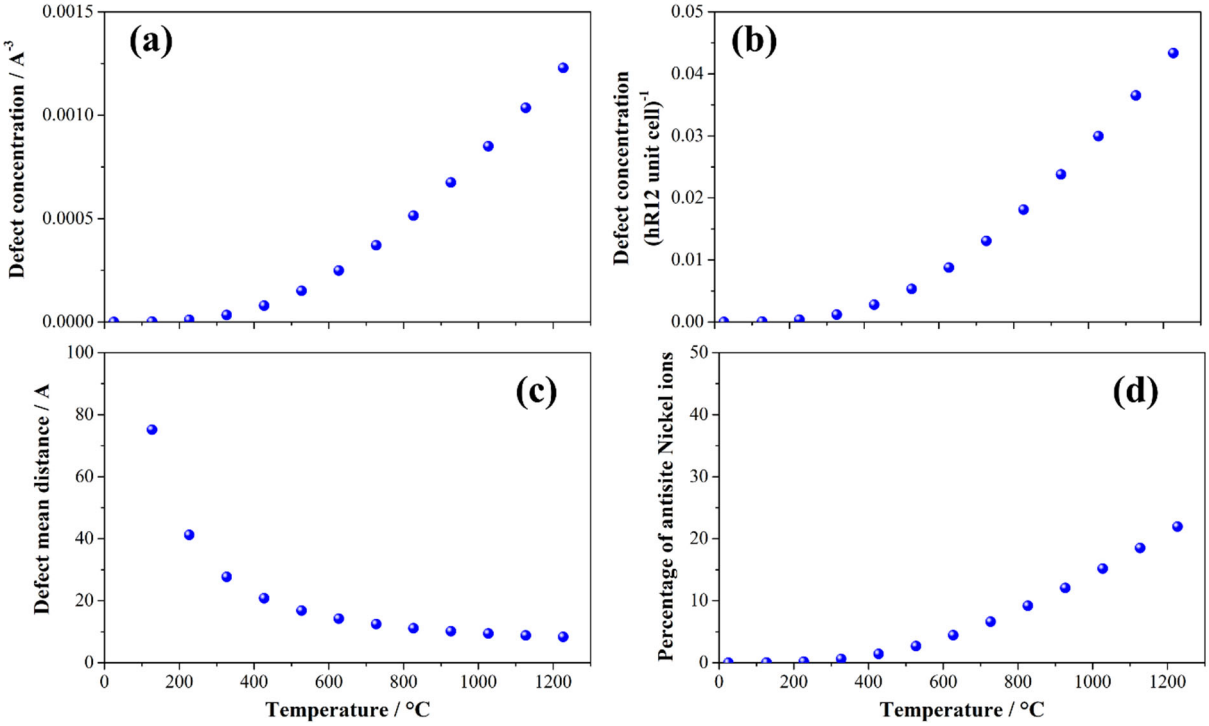

Figure 5. Concentration of the antisite defects in the LRLO lattice normalized (**a**) by formula unit ($C_{antisite}$(f.u.$^{-1}$)) by volume of cell ($C_{antisite}$(Å^{-3})) or (**b**) by volume of cell ($C_{antisite}$(Å^{-3})) as a function of the temperature. (**c**) Estimated mean distance between antisite defects and (**d**) fraction of nickel ions in the LRLO phase that occupied an antisite position.

The analysis of the formation of the Ni/Li antisite in LRLOs as a function of the temperature shows that, in the typical conditions of synthesis of these mixed oxides (700–1000 °C), their concentration is very high, affecting approximately 15% of the total nickel atoms in the structure at 900 °C. As a consequence, at T > 1000 °C the distance between multiple antisite pairs falls below 10 Å. This picture unavoidably leads to extended antisite defectivities occurring in LRLO materials annealed and quenched from T > 800 to 900°C, whereas slow cooling rates likely lead to thermalization and limited antisite concentrations. In this respect, a fine-tuning of the synthesis conditions allows for remarkable control of intrinsic native antisite concentration in the LRLO lattice. However, the very weak variation in lattice constants induced by antisites makes their quantification by XRD difficult, whereas neutron diffraction or X-ray absorption spectroscopy can be valuable experimental tools to evaluate antisite concentrations, both being much more sensitive techniques than XRD in charging alterations close to the metal centers.

It is important to stress that on the one hand, the occurrence of a large concentration of intrinsic Ni/Li antisites can have a detrimental impact on ion transport properties in the lattice, possibly limiting the mobility of Li^+ ions due to the steric hinderance of Ni^{2+}/Ni^{3+} ions in antisites. On the other hand, the presence of Ni^{2+}/Ni^{3+} ions in the Li layer unavoidably contributes to the so-called pillar effect [45] that stabilizes the de-lithiated lattice in highly oxidized conditions, such as the charge state in lithium batteries. This

beneficial effect facilitates a reversible lithium-ion de-insertion/insertion, likely improving the specific capacity and the capacity retention upon cycling. In the experimental literature, the balancing between these two effects is under debate [30,41–43,45], and in consideration of the very diversified possible compositions of LRLOs, it is likely that different balancing between "pillar effect stabilization" and "obstacles to ion diffusion" can occur.

As a final comment, we may speculate about a possible strategy to control or minimize the Ni/Li antisite formation. It is likely that the substitution of Mn^{4+} ions in the TM layer with other larger 4+ cations, even if they are redox-inactive, can mitigate the antisite disorder. In fact, the addition of larger cations in the TM layer can indirectly shrink the NiO_6 octahedra, thus making less favorable the Ni/Li switch.

5. Conclusions

In this manuscript, we illustrated and discussed Ni/Li antisite defect formation in $Li_{1.2}Ni_{0.2}Mn_{0.6}O_2$ by first-principle calculations. The Ni/Li antisite switches occurred in LRLOs, driven by the size similarity of the Ni^{2+} and Li^{+} ions. DFT calculations performed on disordered supercells using the GGA + U method were combined in a simple thermodynamic model to evaluate the temperature dependance of the antisite defect concentration in the lattice and their minimal distance. Our model suggests that Ni/Li switches are likely to occur above 700–800 °C, with the estimated fraction of Ni atoms in antisite crystallographic positions being as large as 15% at 1000°C. Our prediction can support the identification of experimental conditions needed to control the native concentration of intrinsic Ni/Li antisite defects in the LRLO lattice by a fine-tuning of the synthesis parameters. In this view, further experimental or computational studies concerning the impact of native defectivity on the resilience of the LRLO lattice upon lithium de-intercalation are required to decouple the balancing between the beneficial "pillar effect" and the negative hinderance on the lithium transport properties induced by antisites.

Author Contributions: Conceptualization, S.B., O.P. and A.P.; methodology, A.B.M.G. and M.P.; investigation, A.C. (Arcangelo Celeste) and M.T.; writing—original draft preparation, S.B. and M.T.; writing—review and editing, A.B.M.G., A.C. (Angelo Costantini), M.P., O.P. and A.P. All authors have read and agreed to the published version of the manuscript.

Funding: This project received funding from the European Union's Horizon 2020 research and innovation program under grant agreement No. 814464.

Institutional Review Board Statement: Not applicable.

Informed Consent Statement: Not applicable.

Data Availability Statement: Data are available upon request from the corresponding author.

Acknowledgments: Laura Silvestri is acknowledged for fruitful discussions.

Conflicts of Interest: The authors declare no conflict of interest.

References

1. Pierini, A.; Brutti, S.; Bodo, E. Reactive Pathways toward Parasitic Release of Singlet Oxygen in Metal-Air Batteries. *Npj Comput. Mater.* **2021**, *7*, 126. [CrossRef]
2. Meggiolaro, D.; Gigli, G.; Paolone, A.; Vitucci, F.; Brutti, S. Incorporation of Lithium by MgH_2: An Ab Initio Study. *J. Phys. Chem. C* **2013**, *117*, 22467–22477. [CrossRef]
3. Meggiolaro, D.; Gigli, G.; Paolone, A.; Reale, P.; Doublet, M.L.; Brutti, S. Origin of the Voltage Hysteresis of MgH 2 Electrodes in Lithium Batteries. *J. Phys. Chem. C* **2015**, *119*, 17044–17052. [CrossRef]
4. Tuccillo, M.; Palumbo, O.; Pavone, M.; Muñoz-García, A.B.; Paolone, A.; Brutti, S. Analysis of the Phase Stability of $LiMO_2$ Layered Oxides (M = Co, Mn, Ni). *Crystals* **2020**, *10*, 526. [CrossRef]
5. Paolone, A.; Brutti, S. Performances of Different DFT Functionals to Calculate the Anodic Limit of Fluorinated Sulphonyl-Imide Anions for Lithium Cells. In *The Journal of Physics: Conference Series*; IOP Publishing: Bristol, UK, 2021; Volume 2090.
6. di Muzio, S.; Paolone, A.; Brutti, S. Thermodynamics of the Hydrolysis of Lithium Salts: Pathways to the Precipitation of Inorganic SEI Components in Li-Ion Batteries. *J. Electrochem. Soc.* **2021**, *168*, 100514. [CrossRef]

7. Tuccillo, M.; Mei, L.; Palumbo, O.; Muñoz-García, A.B.; Pavone, M.; Paolone, A.; Brutti, S. Replacement of Cobalt in Lithium-Rich Layered Oxides by n-Doping: A Dft Study. *Appl. Sci.* **2021**, *11*, 10545. [CrossRef]
8. ben Yahia, M.; Lemoigno, F.; Rousse, G.; Boucher, F.; Tarascon, J.-M.M.; Doublet, M.-L.L. Origin of the 3.6 V to 3.9 V Voltage Increase in the $LiFeSO_4F$ Cathodes for Li-Ion Batteries. *Energy Environ. Sci.* **2012**, *5*, 9584. [CrossRef]
9. Dalverny, A.-L.; Filhol, J.-S.; Doublet, M.-L. Interface Electrochemistry in Conversion Materials for Li-Ion Batteries. *J. Mater. Chem.* **2011**, *21*, 10134. [CrossRef]
10. Saubanere, M.; McCalla, E.; Tarascon, J.-M.; Doublet, M.-L. The Intriguing Question of Anionic Redox in High-Energy Density Cathodes for Li-Ion Batteries. *Energy Environ. Sci.* **2016**, *9*, 984–991. [CrossRef]
11. Lombardo, T.; Duquesnoy, M.; El-Bouysidy, H.; Årén, F.; Gallo-Bueno, A.; Jørgensen, P.B.; Bhowmik, A.; Demortière, A.; Ayerbe, E.; Alcaide, F.; et al. Artificial Intelligence Applied to Battery Research: Hype or Reality? *Chem. Rev.* **2021**. [CrossRef]
12. Forero-Saboya, J.D.; Tchitchekova, D.S.; Johansson, P.; Palacín, M.R.; Ponrouch, A. Interfaces and Interphases in Ca and Mg Batteries. *Adv. Mater. Interfaces* **2022**, *9*, 2101578. [CrossRef]
13. Armstrong, A.R.; Lyness, C.; Panchmatia, P.M.; Islam, M.S.; Bruce, P.G. The lithium intercalation process in the low-voltage lithium battery anode $Li_{1+x}V_{1-x}O_2$. *Nat. Mater.* **2011**, *10*, 223–229. [CrossRef] [PubMed]
14. Morgan, L.M.; Islam, M.M.; Yang, H.; O'Regan, K.; Patel, A.N.; Ghosh, A.; Kendrick, E.; Marinescu, M.; Offer, G.J.; Morgan, B.J.; et al. From Atoms to Cells: Multiscale Modeling of $LiNi_xMn_yCo_zO_2$ Cathodes for Li-Ion Batteries. *ACS Energy Lett.* **2022**, *7*, 108–122. [CrossRef]
15. Cai, Z.; Ji, H.; Ha, Y.; Liu, J.; Kwon, D.-H.; Zhang, Y.; Urban, A.; Foley, E.E.; Giovine, R.; Kim, H.; et al. Realizing Continuous Cation Order-to-Disorder Tuning in a Class of High-Energy Spinel-Type Li-Ion Cathodes. *Matter* **2021**, *4*, 3897–3916. [CrossRef]
16. Jun, K.J.; Sun, Y.; Xiao, Y.; Zeng, Y.; Kim, R.; Kim, H.; Miara, L.J.; Im, D.; Wang, Y.; Ceder, G. Lithium Superionic Conductors with Corner-Sharing Frameworks. *Nat. Mater.* **2022**. [CrossRef]
17. Yang, J.H.; Kim, H.; Ceder, G. Insights into Layered Oxide Cathodes for Rechargeable Batteries. *Molecules* **2021**, *26*, 3173. [CrossRef]
18. Voronina, N.; Sun, Y.-K.; Myung, S.-T. Co-Free Layered Cathode Materials for High Energy Density Lithium-Ion Batteries. *ACS Energy Lett.* **2020**, *5*, 1814–1824. [CrossRef]
19. Divakaran, A.M.; Minakshi, M.; Bahri, P.A.; Paul, S.; Kumari, P.; Divakaran, A.M.; Manjunatha, K.N. Rational Design on Materials for Developing next Generation Lithium-Ion Secondary Battery. *Prog. Solid State Chem.* **2021**, *62*, 100298. [CrossRef]
20. Ferro, P.; Bonollo, F. Materials Selection in a Critical Raw Materials Perspective. *Mater. Des.* **2019**, *177*, 107848. [CrossRef]
21. *European Commission Methodology for Establishing the EU List of Critical Raw Materials*; Publications Office of the European Union: Luxembourg, 2017.
22. Simonelli, L.; Sorrentino, A.; Marini, C.; Ramanan, N.; Heinis, D.; Olszewski, W.; Mullaliu, A.; Birrozzi, A.; Laszczynski, N.; Giorgetti, M.; et al. Role of Manganese in Lithium- and Manganese-Rich Layered Oxides Cathodes. *J. Phys. Chem. Lett.* **2019**, *10*, 3359–3368. [CrossRef]
23. Celeste, A.; Tuccillo, M.; Santoni, A.; Reale, P.; Brutti, S.; Silvestri, L. Exploring a Co-Free, Li-Rich Layered Oxide with Low Content of Nickel as a Positive Electrode for Li-Ion Battery. *ACS Appl. Energy Mater.* **2021**, *4*, 11290–11297. [CrossRef]
24. Celeste, A.; Brescia, R.; Greco, G.; Torelli, P.; Mauri, S.; Silvestri, L.; Pellegrini, V.; Brutti, S. Pushing Stoichiometries of Lithium-Rich Layered Oxides Beyond Their Limits. *ACS Appl. Energy Mater.* **2022**, *5*, 1905–1913. [CrossRef] [PubMed]
25. Jarvis, K.A.; Deng, Z.; Allard, L.F.; Manthiram, A.; Ferreira, P.J. Atomic Structure of a Lithium-Rich Layered Oxide Material for Lithium-Ion Batteries: Evidence of a Solid Solution. *Chem. Mater.* **2011**, *23*, 3614–3621. [CrossRef]
26. Lo, W.-T.; Yu, C.; Leggesse, E.G.; Nachimuthu, S.; Jiang, J.-C. Understanding the Role of Dopant Metal Atoms on the Structural and Electronic Properties of Lithium-Rich $Li_{1.2}Mn_{0.6}Ni_{0.2}O_2$ Cathode Material for Lithium-Ion Batteries. *J. Phys. Chem. Lett.* **2019**, *10*, 4842–4850. [CrossRef] [PubMed]
27. Wu, F.; Kim, G.-T.; Diemant, T.; Kuenzel, M.; Schür, A.R.; Gao, X.; Qin, B.; Alwast, D.; Jusys, Z.; Behm, R.J.; et al. Reducing Capacity and Voltage Decay of Co-Free Li1.2Ni0.2Mn0.6O2 as Positive Electrode Material for Lithium Batteries Employing an Ionic Liquid-Based Electrolyte. *Adv. Energy Mater.* **2020**, *10*, 2001830. [CrossRef]
28. Ren, Q.; Xie, H.; Wang, M.; Ding, X.; Cui, J.; Luo, D.; Liu, C.; Lin, Z. Deciphering the Effects of Hexagonal and Monoclinic Structure Distribution on the Properties of Li-Rich Layered Oxides. *Chem. Commun.* **2021**, *57*, 3512–3515. [CrossRef]
29. Nakamura, T.; Gao, H.; Ohta, K.; Kimura, Y.; Tamenori, Y.; Nitta, K.; Ina, T.; Oishi, M.; Amezawa, K. Defect Chemical Studies on Oxygen Release from the Li-Rich Cathode Material $Li_{1.2}Mn_{0.6}Ni_{0.2}O_{2-\delta}$. *J. Mater. Chem. A* **2019**, *7*, 5009–5019. [CrossRef]
30. Jarvis, K.A.; Deng, Z.; Allard, L.F.; Manthiram, A.; Ferreira, P.J. Understanding Structural Defects in Lithium-Rich Layered Oxide Cathodes. *J. Mater. Chem.* **2012**, *22*, 11550–11555. [CrossRef]
31. Xie, Y.; Meng, S.; Chen, X.; Liang, X.; Jin, Y.; Xiang, L. Synergetic Effect of High Ni Ratio and Low Oxygen Defect Interface Zone of Single Crystals on the Capacity Retention of Lithium Rich Layered Oxides. *J. Colloid Interface Sci.* **2021**, *594*, 485–492. [CrossRef]
32. Bareño, J.; Balasubramanian, M.; Kang, S.H.; Wen, J.G.; Lei, C.H.; Pol, S.; Petrov, I.; Abraham, D.P. Long-Range and Local Structure in the Layered Oxide $Li_{1.2}Co_{0.4}Mn_{0.4}O_2$. *Chem. Mater.* **2011**, *23*, 2039–2050. [CrossRef]
33. Li, Y.; Li, Z.; Chen, C.; Yang, K.; Cao, B.; Xu, S.; Yang, N.; Zhao, W.; Chen, H.; Zhang, M.; et al. Recent Progress in Li and Mn Rich Layered Oxide Cathodes for Li-Ion Batteries. *J. Energy Chem.* **2021**, *61*, 368–385. [CrossRef]
34. Koyama, Y.; Arai, H.; Tanaka, I.; Uchimoto, Y.; Ogumi, Z. High Temperature Defect Chemistry in Layered Lithium Transition-Metal Oxides Based on First-Principles Calculations. *J. Power Sources* **2013**, *244*, 592–596. [CrossRef]

35. Wang, Z.; Lin, X.; Zhang, J.; Wang, D.; Ding, C.; Zhu, Y.; Gao, P.; Huang, X.; Wen, G. Spherical Layered Li-Rich Cathode Material: Unraveling the Role of Oxygen Vacancies on Improving Lithium Ion Conductivity. *J. Power Sources* **2020**, *462*, 228171. [CrossRef]
36. Wu, F.; Kim, G.-T.; Kuenzel, M.; Zhang, H.; Asenbauer, J.; Geiger, D.; Kaiser, U.; Passerini, S. Elucidating the Effect of Iron Doping on the Electrochemical Performance of Cobalt-Free Lithium-Rich Layered Cathode Materials. *Adv. Energy Mater.* **2019**, *9*, 1902445. [CrossRef]
37. Yu, H.; Kim, H.; Wang, Y.; He, P.; Asakura, D.; Nakamura, Y.; Zhou, H. High-Energy "composite" Layered Manganese-Rich Cathode Materials via Controlling Li_2MnO_3 Phase Activation for Lithium-Ion Batteries. *Phys. Chem. Chem. Phys.* **2012**, *14*, 6584–6595. [CrossRef]
38. Boulineau, A.; Gutel, T. Revealing Electrochemically Induced Antisite Defects in $LiCoPO_4$: Evolution upon Cycling. *Chem. Mater.* **2015**, *27*, 802–807. [CrossRef]
39. Hu, J.; Xiao, Y.; Tang, H.; Wang, H.; Wang, Z.; Liu, C.; Zeng, H.; Huang, Q.; Ren, Y.; Wang, C.; et al. Tuning Li-Ion Diffusion in α-LiMn1–XFexPO4 Nanocrystals by Antisite Defects and Embedded β-Phase for Advanced Li-Ion Batteries. *Nano Lett.* **2017**, *17*, 4934–4940. [CrossRef]
40. Maier, J.; Amin, R. Defect Chemistry of LiFePO4. *J. Electrochem. Soc.* **2008**, *155*, A339. [CrossRef]
41. Jamil, S.; Li, C.; Fasehullah, M.; Liu, P.; Xiao, F.; Wang, H.; Bao, S.; Xu, M. Ni/Li Antisite Induced Disordered Passivation Layer for High-Ni Layered Oxide Cathode Material. *Energy Storage Mater.* **2022**, *45*, 720–729. [CrossRef]
42. Tang, Z.; Wang, S.; Liao, J.; Wang, S.; He, X.; Pan, B.; He, H.; Chen, C. Facilitating Lithium-Ion Diffusion in Layered Cathode Materials by Introducing Li + /Ni 2+ Antisite Defects for High-Rate Li-Ion Batteries. *Research* **2019**, *2019*, 2198906. [CrossRef]
43. Hoang, K.; Johannes, M. Defect Physics and Chemistry in Layered Mixed Transition Metal Oxide Cathode Materials: (Ni, Co, Mn) vs. (Ni, Co, Al). *Chem. Mater.* **2016**, *28*, 1325–1334. [CrossRef]
44. Kandhasamy, S.; Nallathamby, K.; Minakshi, M. Role of Structural Defects in Olivine Cathodes. *Prog. Solid State Chem.* **2012**, *40*, 1–5. [CrossRef]
45. Liang, J.; Wu, D.; Hu, M.; Tian, Y.; Wei, J.; Zhou, Z. Could Li/Ni Disorder Be Utilized Positively? Combined Experimental and Computational Investigation on Pillar Effect of Ni at Li Sites on LiCoO2 at High Voltages. *Electrochim. Acta* **2014**, *146*, 784–791. [CrossRef]
46. Li, F.; Liu, Z.; Shen, J.; Xu, X.; Zeng, L.; Zhang, B.; Zhu, H.; Liu, Q.; Liu, J.; Zhu, M. A Nanorod-like Ni-Rich Layered Cathode with Enhanced Li+ Diffusion Pathways for High-Performance Lithium-Ion Batteries. *J. Mater. Chem. A* **2021**, *9*, 2830–2839. [CrossRef]
47. Li, F.; Liu, Z.; Shen, J.; Xu, X.; Zeng, L.; Li, Y.; Zhang, D.; Zuo, S.; Liu, J. Ni-Rich Layered Oxide with Preferred Orientation (110) Plane as a Stable Cathode Material for High-Energy Lithium-Ion Batteries. *Nanomaterials* **2020**, *10*, 2495. [CrossRef]
48. Xie, Y.; Jin, Y.; Xiang, L. Li-Rich Layered Oxides: Structure, Capacity and Voltage Fading Mechanisms and Solving Strategies. *Particuology* **2022**, *61*, 1–10. [CrossRef]
49. Li, Y.; Li, W.; Shimizu, R.; Cheng, D.; Nguyen, H.; Paulsen, J.; Kumakura, S.; Zhang, M.; Meng, Y.S.; Li, Y.; et al. Elucidating the Effect of Borate Additive in High-Voltage Electrolyte for Li-Rich Layered Oxide Materials. *Adv. Energy Mater.* **2022**, *12*, 2103033. [CrossRef]
50. Jarvis, K.; Wang, C.-C.; Varela, M.; Unocic, R.R.; Manthiram, A.; Ferreira, P.J. Surface Reconstruction in Li-Rich Layered Oxides of Li-Ion Batteries. *Chem. Mater* **2017**, *29*, 7668–7674. [CrossRef]
51. Chen, C.-J.; Kong, W.; Mori, T.; Peterson, V.K.; Sharma, N.; Lee, P.-H.; Wu, S.-H.; Wang, C.-C.; Song, Y.-F.; Liu, R.-S. The Origin of Capacity Fade in the Li_2 MnO_3 $LiMO_2$ (M = Li, Ni, Co, Mn) Microsphere Positive Electrode: An Operando Neutron Diffraction and Transmission X-ray Microscopy Study. *J. Am. Chem. Soc.* **2016**, *138*, 8824–8833. [CrossRef]
52. Kugel, K.I.; Khomskii, D.I. The Jahn-Teller Effect and Magnetism: Transition Metal Compounds. *Sov. Phys. Uspekhi* **1982**, *25*, 621–641. [CrossRef]
53. Shannon, R.D.; Prewitt, C.T. Effective Ionic Radii in Oxides and Fluorides. *Acta Cryst.* **1969**, *B25*, 925–946. [CrossRef]
54. Shannon, R.D. Revised Effective Ionic Radii and Systematic Studies of Interatomic Distances in Halides and Chalcogenides. *Acta Crystallogr.* **1976**, *A32*, 751–767. [CrossRef]
55. Minakshi, M.; Singh, P.; Appadoo, D.; Martin, D.E. Synthesis and Characterization of Olivine $LiNiPO_4$ for Aqueous Rechargeable Battery. *Electrochim. Acta* **2011**, *56*, 4356–4360. [CrossRef]
56. Ivanova, S.; Zhecheva, E.; Stoyanova, R.; Nihtianova, D.; Wegner, S.; Tzvetkova, P.; Simova, S. High-Voltage $LiNi_{1/2}Mn_{3/2}O_4$ Spinel: Cationic Order and Particle Size Distribution. *J. Phys. Chem. C* **2011**, *115*, 25170–25182. [CrossRef]
57. Chi, L.H.L.H.; Dinh, N.N.N.N.; Brutti, S.; Scrosati, B. Synthesis, Characterization and Electrochemical Properties of 4.8 V LiNi0.5Mn1.5O4 Cathode Material in Lithium-Ion Batteries. *Electrochim. Acta* **2010**, *55*, 5110–5116. [CrossRef]